



Study of *in vitro* bioactivity of biogenic hydroxyapatite synthesized from Black Sea *Rapana venosa* shells

Milena Nedkova-Shtipska, Irena Mihailova[®], Hristo Georgiev, Albena Yoleva, Aneliya Petrina*

University of Chemical Technology and Metallurgy 8 Kliment Ohridski Blvd., 1797 Sofia, Bulgaria

Received 4 July 2025; Received in revised form 11 September 2025; Accepted 22 September 2025

Abstract

The biogenic hydroxyapatite (BHA) used in this study was synthesized via solid-state reaction from Rapana venosa shells - a natural CaO source and monocalcium phosphate monohydrate $Ca(H_2PO_4)_2 \cdot H_2O$. The in vitro bioactivity of the synthesized BHA was evaluated in simulated body fluid (SBF) over 4, 7, 15 and 21 days (Kokubo protocol). After exposure to SBF, surface changes of the BHA samples and the ion exchange dynamics with the medium were analysed using different methods. Fourier-transform infrared spectroscopy analyses confirmed the stability of the phosphate structure of the BHA samples and the formation of apatite-like layers. The vibration modes of PO_4^{3-} tetrahedral are studied through Raman spectroscopy for all the analysed powders. Scanning electron microscopy images revealed increasing mineralization of the BHA samples in interaction with SBF in period of up to 15–21 days, evidenced by the formation and densification of the surface crystalline phase. Energy-dispersive X-ray spectroscopy analysis confirmed rising and stabilization of Ca/P content, corresponding to the secondary apatite formation. Inductively coupled plasma optical emission spectroscopy (ICP-OES) results indicated changes in Ca^{2+} and PO_4^{3-} concentrations in the SBF solution, confirming dissolution and precipitation dynamics. The results demonstrate a good bioactivity of the synthesized BHA and its potential for bone tissue engineering applications.

Keywords: biogenic hydroxyapatite, Rapana venosa, bioactivity, biomineralization

I. Introduction

Hydroxyapatite (HAp, $Ca_{10}(PO_4)_6(OH)_2$) is one of the most preferred bioactive materials due to its composition, biocompatibility and osteoinductive and osseointegration capabilities, which closely resembles those of natural bone and dental tissues [1–3]. Consequently, it is widely used in medicine and dentistry for applications such as bone grafts and reconstruction, implant coatings and more, providing a dynamic chemical bond at the interface with the host tissue [4,5].

The remarkable structure of hydroxyapatite (HAp) allows for substitutions of both cations and anions, leading to the enhancement of the resulting biomaterials' properties. Replacing calcium ions with various metal ions such as zinc, copper, silver, etc. improves the mechanical performance of the materials and imparts targeted properties, including antimicrobial ac-

ies have been conducted on the effects of ionic doping on the biological and functional properties of HAp for bone repair in dentistry and cancer treatment. Cimpeanu et al. [6] investigated the biocompatibility and antimicrobial properties of magnesium-doped hydroxyapatite and amoxicillin-enriched HAp synthesized via an innovative adaptive co-precipitation method. The materials exhibited excellent biocompatibility and effective antimicrobial properties against S. aureus, E. coli, and C. albicans, indicating their suitability for biomedical applications. The antibacterial properties, biological activity, and optical characteristics of nanohydroxyapatite are enhanced by incorporating copper, strontium, and lanthanides. Doping nanohydroxyapatite with Mg²⁺ ions improves adhesive capacity and imparts antibiofilm properties [7,8]. Coatings of chromium-doped hydroxyapatite with incorporated amoxicillin demonstrated physicochemical properties similar to those of pure hydroxyapatite but with higher biological activ-

tivity and enhanced biocompatibility. Numerous stud-

*Corresponding author: +35 928163377

e-mail: apetrina@uctm.edu

ity [9]. The biocompatibility of the coatings was evaluated using the MG63 cell line, revealing a high percentage of viable cells, indicative of good cell proliferation without adverse cytotoxic effects. Nanocomposite coatings of chromium-doped hydroxyapatite have also demonstrated excellent antibacterial and antifungal activity [10].

HAp has proven to be a versatile carrier for the delivery and controlled release of drugs, cells, and bioactive molecules. Porous microspheres of F⁻ substituted hydroxyapatite, synthesized via a hydrothermal method, have shown potential for application as fluoride-releasing bioactive carriers in the treatment of osteoporosis and bone defects [11].

In recent years, different approaches have been developed for synthesizing biogenic hydroxyapatite (BHA) from natural waste materials such as corals, seashells, eggshells, and snails [12-15]. The use of natural products reduces production costs and environmental pollution from biological waste, making this approach a sustainable and eco-friendly alternative. These resources are excellent calcium (Ca) and phosphorus (P) precursors, as they contain essential ions inherent to biological HAp. Unlike synthetic HAp, BHA is nonstoichiometric, containing trace elements such as Na⁺, Zn²⁺, Mg²⁺, K⁺, Si⁴⁺, Ba²⁺, F⁻, and CO₃²⁻, which makes its chemical composition closer to that of human bone. Biogenic apatites are further characterized by small crystallite sizes and low crystallinity, combined with non-stoichiometry, lattice defects, and the presence of carbonate ions in the crystal lattice, which together account for their specific properties. These structural features are crucial for bioactivity and bone adhesion [10,16,17].

Despite their excellent bioactive properties, pure forms of synthesized BHA typically exhibit poor mechanical strength [5,8,12]. To overcome this limitation, reinforcement strategies are often employed, including composite formation, coating integration with metallic implants, or polymer encapsulation. Such approaches optimize the balance between mechanical strength and osseointegration, enabling successful bone repair. Sampath and Krishnasamy [18] proposed a green synthesis of self-organized hydroxyapatite nanocomposites on graphene oxide sheets derived from seashell waste for regenerative medicine. The synthesized BHA nanorods were reinforced with carbon nanotubes and chitosan on graphene oxide sheets, supported by a polylactic acid polymer matrix. This eliminated brittleness and imperfect self-assembly, improving the strength and toughness of the material. The resulting porous composites exhibited high hardness, tensile strength, and excellent cell viability, highlighting their potential for bone tissue engineering [18].

An effective initial assessment of BHA bioactivity can be performed using the classical procedure proposed by Kokubo [19] as well as some other researches [20–23], which involves the contact of bioactive ceramics with a simulated body fluid (SBF). Hussain *et al.*

[24] reported the successful synthesis of BHA coatings from Indian mussel shells via a hydrothermal method at different temperatures. In a subsequent study, the team demonstrated the in vitro bioactivity of the obtained coatings through immersion in simulated body fluid (SBF test) [25]. Biocompatibility studies of the BHA coatings via MTT assay with human osteosarcoma MG63 cells demonstrated enhanced cell density [25]. The synthesis conditions and the type of biogenic precursors are important factors influencing the structure and bioactivity of the resulting BHA. A comparative study of the structural, functional, and thermal stability, as well as the morphological characteristics of three types of composites derived from natural calcium precursors (seashells, coral skeletons, and eggshells) containing nanohydroxyapatite and polyvinyl alcohol, was conducted by Jeyakumar et al. [26]. The SBF test revealed that the bioactivity of the biocomposites varied depending on the precursor in the following order: coral > seashell > eggshell. The rate and extent of surface coverage with a newly formed apatite layer followed the same trend. Forero-Sossa et al. [12] investigated the influence of source and processing methodologies on the physicochemical properties and bioactive response of BHA powders derived from bovine and porcine bones. The results underscore the significant impact of the synthesis method on the structure and bioactivity of BHA.

The BHA powder used in the present study was synthesized by a solid-state reaction from Rapana venosa shells, an invasive species rich in $CaCO_3$ found along the Black Sea coast-and monocalcium phosphate, $Ca(H_2PO_4)_2 \cdot H_2O$. The chemical and phase composition of Rapana venosa shells, as well as the synthesis and structural characterization of the resulting BHA, have been reported elsewhere [27,28].

The aim of this study is to investigate the time-dependent surface transformation of BHA derived from Black Sea *Rapana venosa* shells in simulated body fluid as a criterion for evaluating the *in vitro* bioactivity of the material.

II. Experimental

2.1. Sample preparation

The biogenic hydroxyapatite used in this study was synthesized via solid state reaction using shells of *Rapana venosa* (a biogenic CaO source) and monocalcium phosphate monohydrate $Ca(H_2PO_4)_2 \cdot H_2O$ at 1180 °C with a hold of 2 h at the maximum temperature.

The powdered shells of *Rapana venosa* consist of approximately 98 wt.% CaCO₃, predominantly in the form of calcite with minor amounts of aragonite (according to X-ray diffraction analysis). The decomposition of calcium carbonate begins above 800 °C and at 900 °C most of the carbonate is decomposed to CaO, while at 1000 °C almost complete decarbonization is achieved, yielding about 95 wt.% CaO and ~5 wt.% portlandite [27].

For the synthesis of hydroxyapatite, the shells were crushed and milled in a ball mill to a particle size below 63 µm. The obtained powder was calcined at 1000 °C for 1 h to CaO. Monocalcium phosphate monohydrate, $Ca(H_2PO_4)_2 \cdot H_2O$, was also calcined at 1000 °C and sieved to a particle size <63 μm. Calcination of the raw materials at elevated temperature increases their reactivity and facilitates the development of a well-ordered crystalline structure. Subsequently, the two powders were homogenized in a ball mill in a 1:1 weight ratio and uniaxially pressed into pellets (\emptyset 3 \times 0.5 cm) under a pressure of 50 MPa. The green compacts were sintered at 1180 °C (based on literature data) with a 2h dwell at the peak temperature to complete the solid-solid reaction and to ensure high crystallinity with reduced defect density [28]. The sintered specimens were then ground into powder. The synthesized biogenic hydroxyapatite was characterized using Xray diffraction (XRD), Fourier-transform infrared spectroscopy (FTIR), scanning electron microscopy (SEM) and energy-dispersive X-ray spectroscopy (EDS).

The classical method for rapid assessment of surface bioactivity in biogenic hydroxyapatite was proposed by Kokubo [19] as well as some other researches [20–23], who suggested the using of simulated body fluid (SBF), an ionic solution resembling human blood plasma in composition. Immersing synthesized bioactive materials in SBF for specific periods under controlled conditions leads to the formation of a carbonate-containing hydroxyapatite layer on their surfaces (Kokubo protocol). The dynamics of ion exchange between the medium and the material's surface, as well as the rate of hydroxyapatite layer formation, serve as indicators of the synthesized biogenic hydroxyapatite bioactivity.

The *in vitro* bioactivity of the hydroxyapatite derived from *Rapana venosa* shells (BHA) was investigated in SBF over 4, 7, 15 and 21 days and the obtained samples were denoted as BHA 4d SBF, BHA 7d SBF, BHA 15d SBF and BHA 21d SBF, respectively. After the SBF test, the BHA and liquid samples were subjected to a series of analyses (FTIR, Raman, SEM-EDS and ICP-OES) to determine the phase composition of the contact surface and the ion exchange between the ceramic and SBF.

2.2. Characterization

SBF test - The SBF test for evaluating the bioactive behaviour of the synthesized BHA was conducted in a simulated body fluid (SBF) with pH 7.4 at 37 °C in a water bath, following the Kokubo protocol, over 4, 7, 15 and 21 days. The BHA powder (0.2 g) was pressed (at 12 MPa) into pellets with diameter of 10 mm and thickness of 0.5 mm. Two samples were placed in polyethylene containers containing 40 ml of SBF solution. The surface area to volume (S_A/V) ratio of the samples to the SBF was $0.1 \, \mathrm{cm}^{-1}$.

Fourier-transform infrared spectroscopy (FTIR) - Surface functional group changes during the SBF test were analysed using a Varian 660 FTIR Spectrometer

(Agilent Technologies Inc., USA) with Resolution Pro[®] software. The spectra were recorded in the mid-IR range (4000–400 cm⁻¹, with 4 cm⁻¹ resolution) in transmission mode. The powdered BHA was mixed with KBr for spectral analysis and pressed into pellets.

Raman spectroscopy - All spectra were collected with a RENISHAW inVia Raman microscope Raman spectrometer equipped with an inVia Qontor Microscope with Leica objectives and CCD detector. For detection of vibrational modes of PO₄³⁻ laser with wavelength 532 nm and 1800 l/mm (vis) grating was used. The maximum power at the output of the laser head was 5 mW. The spectra of the samples placed in a glass substrate (2 mm) were recorded with 2 cm⁻¹ resolution and five accumulations of 10000 ms exposure time each at laser power mentioned above in the range 100–3700 cm⁻¹ using the WiRE 5.6 software. To focus the laser beam and collect the scattered light in a backscattering configuration, an ×50 objective was used. The diameter of the illuminated spot on the sample surface was about 1 µm. The temperature of the air in the laboratory was 21 °C and the Raman spectrometer was calibrated with internal silicon sample and observed peak at 521 cm⁻¹.

Scanning Electron Microscopy (SEM) - The microstructure and morphology of the samples were examined using a Tescan FIBSEM LYRA scanning electron microscope (TESCAN GROUP, a.s, Czech Republic), at 20 kV. The system was equipped with an energy-dispersive X-ray spectroscopy (EDS) detector for compositional analysis.

Inductively coupled plasma optical emission spectrometry (ICP-OES) - ICP-OES was used to evaluate ion exchange dynamics between the BHA and SBF medium. The analysis was performed using a High Dispersion ICP-OES Prodigy spectrometer (Teledyne Leeman Labs, USA) with an Eschelle optical system and a L-PAD (Large Format Programmable Array Detector). The analysis was carried out in the 165–1100 nm spectral range with a resolution of 0.007 nm, in argon flow, allowing for spectral line correction. Accuracy was verified using control samples (blanks and standards). A multielement standard solution was used. This method was also used to experimentally determine the chemical composition of the initial BHA after acid decomposition of the sample.

The expanded uncertainty includes the measurement uncertainty and corresponds to a confidence level of approximately 95%.

Loss on ignition (LOI) and moisture content were determined according to the Bulgarian standard BDS 11330:1987, the standard method for LOI determination.

III. Results and discussion

The chemical composition of the BHA (Table 1) shows that the obtained material contains a high percentage of calcium and phosphorus, along with small amounts of accompanying oxides. These elements re-

Table 1. Chemical composition of BHA

Component	Content [wt.%]			
Al ₂ O ₃	1.30 ± 0.08			
BaO	< 0.01			
CaO	54.39 ± 2.74			
Fe_2O_3	1.07 ± 0.07			
K_2O	< 0.05			
MgO	0.50 ± 0.04			
MnO	0.06 ± 0.02			
Na_2O	0.47 ± 0.06			
P_2O_5	40.16 ± 2.08			
SO_3	1.62 ± 0.22			
SiO_2	0.49 ± 0.06			
SrO	0.12 ± 0.03			
TiO_2	0.02 ± 0.01			
ZrO_2	< 0.01			
Loss on ignition	< 0.02			
Moisture	0.04 ± 0.02			

flect the natural origin of the raw materials used for synthesis (*Rapana venosa* shells). The SEM analysis of the BHA sample showed [28] a homogeneous porous structure with a grain size below $10\,\mu m$. Idiomorphic crystals of various sizes are observed, with a predominance of those having size of $4–5\,\mu m$.

3.1. FTIR spectroscopy

FTIR spectroscopy, a well-established method for tracking structural changes and surface modifications, was used to analyse the BHA samples after immersion in simulated body fluid for 4, 7, 15 and 21 days (Fig. 1). The absorption bands of the synthesized biogenic hydroxyapatite are discussed in detail in our previous paper [28]. The spectra exhibit the composite band of asymmetric stretching vibrations of phosphate groups

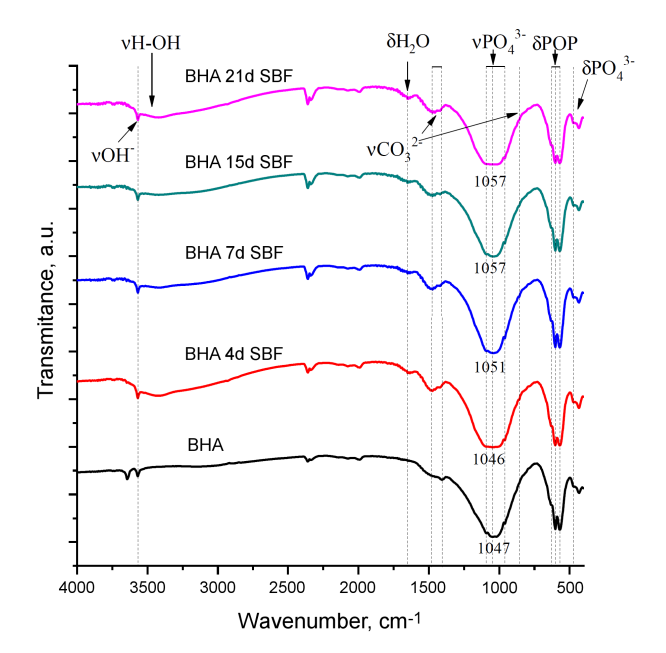


Figure 1. Comparative FTIR spectra of synthesized BHA and BHA samples after immersion in SBF for 4, 7, 15 and 21 days

($ν_{as}$ PO₄³⁻) in the 1090–1040 cm⁻¹ region and a shoulder corresponding to symmetric stretching ($ν_s$ PO₄³⁻-) near 960 cm⁻¹. Absorption bands for bending vibration of δ P–O–P bond at 741 cm⁻¹ and deformation modes (δ PO₄³⁻-) around 630–560 cm⁻¹ [28,29] are also visible. A broad absorption band at 1410–1455 cm⁻¹ in spectrum of the initial BHA is attributed to the carbonate group stretching vibration (ν CO₃²⁻), with a weak shoulder ~880–860 cm⁻¹ [11,30]. Sharp absorption bands for hydroxyl stretching (ν OH⁻) are present at ~3650 and 3550 cm⁻¹, while a weak bend mode for H–O–H (δ HOH) appears near 1624 cm⁻¹ [11,31].

The evolution of the intensity, area and shape of the absorption band of the asymmetric stretching vibrations of the phosphate group ($v_{as} PO_4^{3-}$) can be traced during the interaction of the BHA sample with simulated body fluid (SBF) over time, serving as a specific indicator of the formation and transformation of the apatite layer. For the BHA 4d SBF sample, the change is noticeable not so much in the intensity of the band at $\sim 1050 \,\mathrm{cm}^{-1}$, but rather in its width. The observed broadening is from 10 a.u. (full width at half maximum, FWHM) for the BHA to 13 a.u. for the BHA 4d SBF sample. The absorption band area increases from 12047 a.u. for the initial sample to 13445 a.u. for the BHA 4d SBF. The change in the shape and magnitude of the $(v_{as} PO_4^{3-})$ band reflects the initial phase of the surface degradation of BHA and the enhanced ionic exchange with the medium, associated with an increase in the amorphized fraction. The subsequent rapid adsorption of ions induces local non-equilibrium states within the crystal lattice of the newly formed apatite nuclei.

A visually noticeable increase in the band intensity is observed for the BHA 7d SBF and BHA 15d SBF samples, where a narrowing of the absorption peak to 10 and 11 a.u. is also recorded. This is attributed to the transformation of the primary precipitates into crystalline aggregates with well-ordered structure and the formation of a dense apatite layer. The peak area increases to 14183 a.u. for the BHA 7d SBF and 15049 a.u. for the BHA 15d SBF sample. The increase in the crystallinity of the forming apatite layer on the BHA surface was found up to the 15th day of soaking the BHA samples in SBF. The intensity of the $(v_{as} PO_4^{3-})$ band for the BHA 21d SBF is visually more comparable to that for the BHA sample. The band itself visibly broadens (to 12 a.u.) compared to that in the BHA 7d SBF and BHA 15d SBF spectra and its area slightly decreases to 14828 a.u. This behaviour may be related with the deposition of secondary apatite aggregates or the formation of smaller apatite crystallites with an irregular structure.

Simultaneously, for all SBF tested samples, the intensity of the carbonate group stretching vibrations at \sim 1420 cm⁻¹ also increases. A slight change is also recorded around 875 cm⁻¹ (ν CO₃²⁻). This confirms carbonate incorporation into the apatite structure, i.e. the formation of carbonated hydroxyapatite (type B), resembling bone tissue [1,32].

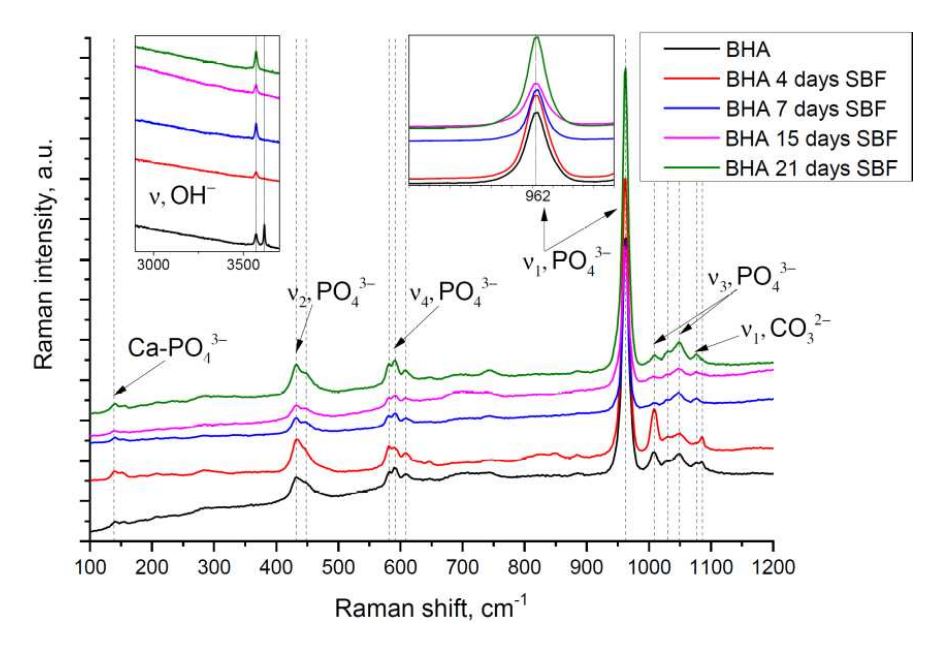


Figure 2. Comparative Raman spectra of synthesized BHA and BHA samples after immersion in SBF for 4, 7, 15 and 21 days

The increase in intensity around $1630\,\mathrm{cm^{-1}}$ and the appearance of a broad band around $3400\,\mathrm{cm^{-1}}$ (δ H₂O and ν OH) reflect the hydrophilicity and the change in the surface chemistry of the BHA samples with increasing immersion time in SBF.

The observed changes in characteristic FTIR absorption bands confirm the formation of an induced apatite layer upon interaction with SBF. This behaviour is typical for bioactive materials and demonstrates the potential of the synthesized BHA for a strong bioactive response.

3.2. Raman spectroscopy

Raman spectroscopy is used and preferred because it is a non-destructive technique that allows analysis of samples without causing damage. It is widely used for the characterization of BHA-based biomaterials.

Figure 2 shows comparison of Raman spectra of all BHA samples after immersion in SBF for 4, 7, 15 and 21 days. The main spectral lines are observed in the 100-3700 cm⁻¹ range, consistent with typical hydroxyapatite (HAp) vibrations. Characteristic phosphate modes include the v_2 vibration at 434 and 450 cm⁻¹, the v_4 vibration at 581 and 608 cm⁻¹, and the ν_1 PO₄³⁻ vibration at 962 cm⁻¹, which are also seen in the literature [33]. There is a small band at 140 cm⁻¹ and it is attributed to Ca-PO₄³⁻ interactions. The peak at 1070 cm⁻¹ corresponds to the v_1 stretching mode of carbonate (CO₃²⁻) in the B position, while the band at 1045 cm⁻¹, which is also associated with carbonate bending, overlaps with the broad background of phosphate v_3 vibrations [33]. The broad band of low-intensity between 3000 and 3750 cm⁻¹ range (see inset in Fig. 2) indicates the presence of trace water within the structure. Additionally, a sharp peak at 3571 cm⁻¹ is attributed to the stretching vibration of the structural OH⁻ group in hydroxyapatite (BHA) [33].

The Raman analysis confirms the observed changes in characteristic FTIR absorption bands and the formation of an induced apatite layer upon interaction with SBF.

3.3. Ion exchange analysis (ICP-OES)

Quantitative determination of ion exchange between the BHA samples and SBF was performed using ICP-OES. The study tracked changes in the concentrations of Ca²⁺, PO₄³⁻, Na⁺, K⁺, Mg²⁺ and Si⁴⁺ ions in the solution after contact with BHA for 4, 7, 15 and 21 days. The focus was on the Ca/P ratio as a measure of the deposition rate of Ca-P layers on the BHA surface, reflecting the bioactivity of the synthesized material. The behaviour of other elements showed minimal changes, primarily indicating the natural and heterogeneous origin of the raw material [2,3], rather than playing a significant role in the formation of the surface BHA layer.

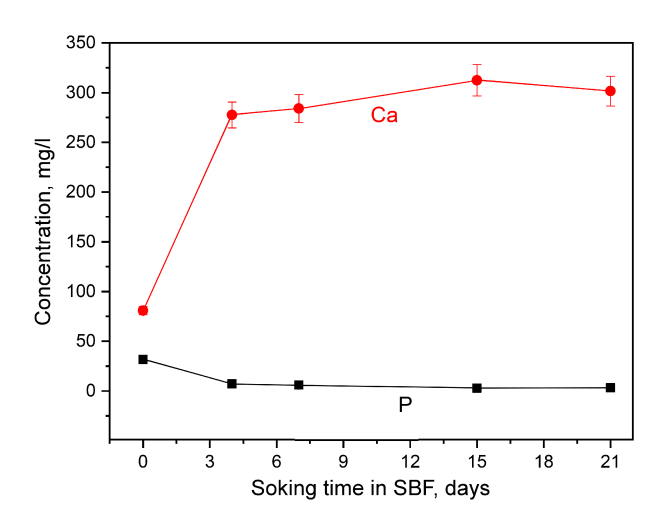


Figure 3. Dynamic changes in Ca²+ and P⁵⁺ concentrations in SBF solutions after soaking of BHA samples for 4, 7, 15 and 21 days

Table 2. ICP-OES analysis of SBF solution after soaking of BHA samples for 4, 7, 15 and 21 days

Sample -	Measured element [mg/l]							
Sample	pН	Mg	Al	Si	S	Na	Fe	
SBF	7.18 ± 0.05 *	36.4 ± 1.8	0.15 ± 0.01	0.74 ± 0.07	27.2 ± 1.4	1866 ± 93.3	0.13 ± 0.01	
BHA 4d	7.94 ± 0.05	43.8 ± 2.2	0.16 ± 0.01	2.01 ± 0.20	36.7 ± 1.8	1724 ± 86.2	0.12 ± 0.01	
BHA 7d	7.84 ± 0.05	44.4 ± 2.3	0.13 ± 0.01	2.43 ± 0.20	37.4 ± 1.9	1703 ± 85.2	0.12 ± 0.01	
BHA 15d	7.76 ± 0.05	44.3 ± 2.3	0.17 ± 0.01	2.65 ± 0.27	37.6 ± 1.9	1752 ± 87.3	0.12 ± 0.01	
BHA 21d	7.69 ± 0.05	44.3 ± 2.3	0.14 ± 0.01	2.98 ± 0.30	36.7 ± 1.8	1786 ± 89.3	0.13 ± 0.01	

*The expanded measurement uncertainties, estimated for ICP-OES analysis in a complex matrix, correspond to a coverage factor of k = 2 ($\approx 95\%$ confidence level)

The results of the ICP-OES analysis of the SBF reactions with BHA for different time periods are presented in Fig. 3 and Table 2.

The results reveal that in the initial days, the ${\rm Ca^{2^+}}$ concentration sharply increased from $80.7\,{\rm mg/l}$ (SBF) to $277.6\,{\rm mg/l}$ (BHA 4d), followed by a plateau ($\sim 300\,{\rm mg/l}$) until day 21 (Fig. 3). This behaviour is characteristic of the initial surface dissolution of BHA (during days 4–7), with rapid calcium release into SBF and the establishment of a dissolution-precipitation balance typical of the early stage of bioactivity. The stabilization after day 4 suggests the formation of new apatite layers that limit further degradation.

Simultaneously, a significant decrease in phosphorus was observed (Fig. 3), from 31.64 mg/l (SBF) to 7.24 mg/l (BHA 4d SBF) and further to 2.80 mg/l (BHA 15d SBF), characteristic of the formation of an apatite-like phase (Ca₁₀(PO₄)₆(OH)₂) on the sample surfaces a clear marker of *in vitro* bioactivity. The lowest values were recorded for the BHA 15d SBF sample, followed by a slight increase, likely due to the surface saturation or the establishment of a dynamic precipitation/desorption equilibrium.

The pH increased from 7.18 (SBF) to 7.94 (BHA 4d SBF), followed by a gradual decline to 7.69 (BHA 21d SBF), reflecting ionic interaction between the SBF and the ceramics. The slight drop after day 4 suggests stabilization of the surface reactions. The moderate pH elevation facilitates apatite precipitation, as phosphate species are more stable in a slightly alkaline medium [34].

The ICP-OES results align with the classic stages of bioactivity in BHA [35]: initial surface dissolution up to day 4 with rapid Ca²⁺ release; followed by precipitation (day 7 onward) with gradual changes in Ca and P concentrations and a slow pH decline. These changes reflect the reorganization of initially formed crystallites and aggregates into a homogeneous microcrystalline structure and layer densification. By day 21, a dense apatite coating on the sample surfaces is formed due to equilibrium between dissolution and deposition.

The involvement of CO_3^{2-} inclusions in the calciumphosphate layer formation suggests the development of a microcrystalline structure, consistent with the changes in the FTIR spectra of the samples. The ion exchange dynamics highlight the pronounced bioactivity of the synthesized BHA.

3.4. SEM/EDS surface morphology and composition

The findings described above are further confirmed by SEM/EDS analysis of the BHA samples (Figs. 4-8). SEM imaging reveals surface morphology and allows a visual evaluation of the material's bioactive behaviour upon exposure to SBF. EDS microanalysis measured the energy distribution and intensity of X-ray signals generated by a focused electron beam on the sample, providing quantitative and qualitative data on the surface components of BHA over time.

Figure 4 shows SEM image of the pristine BHA pellets. The surface appears relatively smooth, with no visible deposits or microstructures. The EDS determined Ca/P ratio of 2.07 is higher than the stoichiometric value (1.67), which is typical for synthetic BHA [36,37]. The excess Ca²⁺ suggests potential for apatite growth. The absence of surface products indicates that biomineralization has not yet begun.

After 4 days of immersion in SBF, SEM images at varying magnifications (Fig. 5) reveal initial spherical formations, primarily along surface irregularities and pore edges, indicating nucleation of an amorphous apatite phase. The Ca/P ratio slightly increases to 2.28, suggesting early surface reactivity with phosphate ion deposition from the solution. The presence of Mg²⁺, Al³⁺, Si⁴⁺, Na⁺ and other ions on the surface signifies ion adsorption from SBF, i.e. initial bioactivity. A slight increase in Mg²⁺ may suggest its inclusion in the

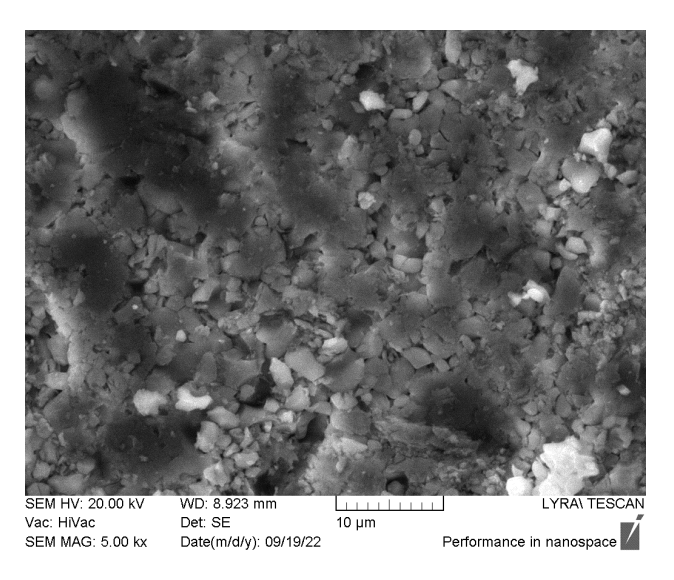


Figure 4. SEM image of the initial BHA sample $\,$

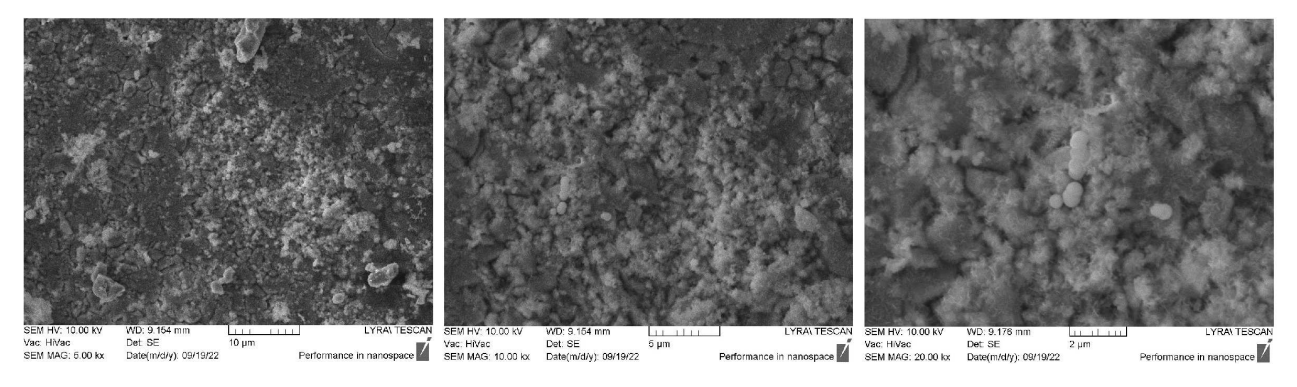


Figure 5. SEM images (different magnifications) of the BHA 4d SBF sample

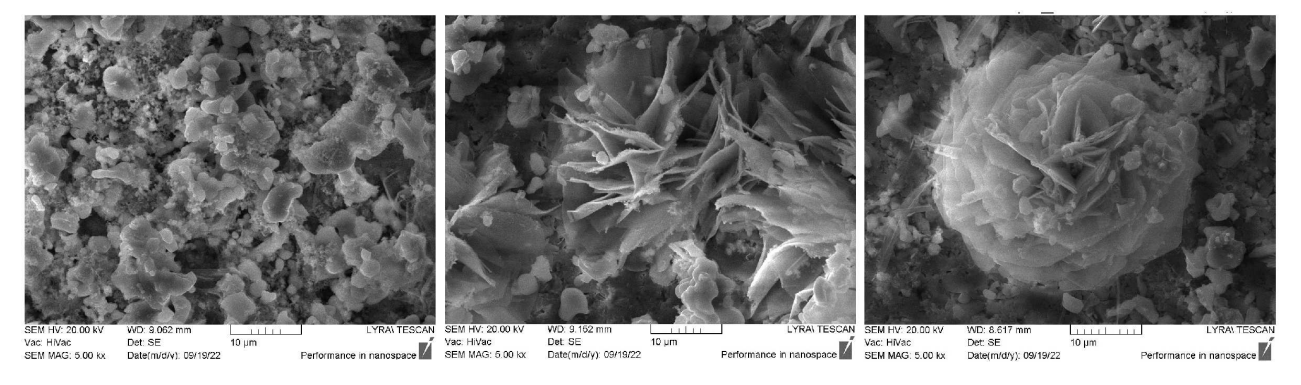


Figure 6. SEM images (different areas) of the BHA 7d SBF sample

amorphous apatite layer, as often seen during the initial phases of biomineralization [38–42].

In the SEM images of the BHA sample soaked for 7 days (Fig. 6), various structures are visible, such as spherules, needle-like crystals and aggregates. All those structures indicate the formation of crystalline apatite layer. Although the surface is not yet fully covered, it shows evident signs of mineralization. The Ca/P ratio = 1.75 is closer to that of biogenic hydroxyapatite, confirming the transformation of the initial amorphous phase into a secondary crystalline apatite layer.

SEM images of selected areas from the 15-day SBF-exposed BHA sample (Fig. 7), show complete surface transformation, with tightly packed spherical and plate-like aggregates nearly covering the original surface. The Ca/P ratio ~1.76 is close to the stoichiometric value, suggesting the development of a stable apatite layer on the ceramic particles. Point-specific SEM/EDS analysis

was also performed (results are not presented here) and confirmed the formation of the multilayered deposits, typical for apatite phase transformation. The measured Ca/P ratio was 1.78 and confirmed the formation of a homogeneous ("mature") apatite surface.

Figure 8 shows SEM images of surface areas and specific points from the 21-day SBF-immersed BHA sample. A dense apatite layer with complex morphology is observed, featuring both homogeneous fine crystallites and secondary flower-like aggregates. EDS analysis confirms a stable elemental composition with Ca/P ratios between 1.77–1.81, characteristic of bioactive apatite.

The change in the atomic Ca/P ratio with immersion time in SBF, reflects the processes occurring on the surface of the BHA samples. The initial increase in Ca/P from 2.07 for BHA to 2.28 for BHA 4d SBF is a result of surface dissolution of the sample in the early

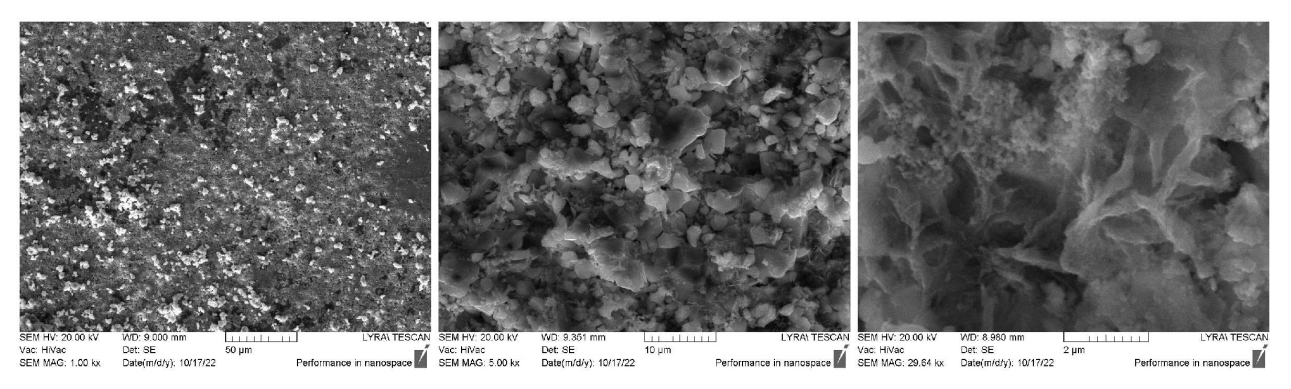


Figure 7. SEM images (different magnifications) of the BHA after 15 days in SBF

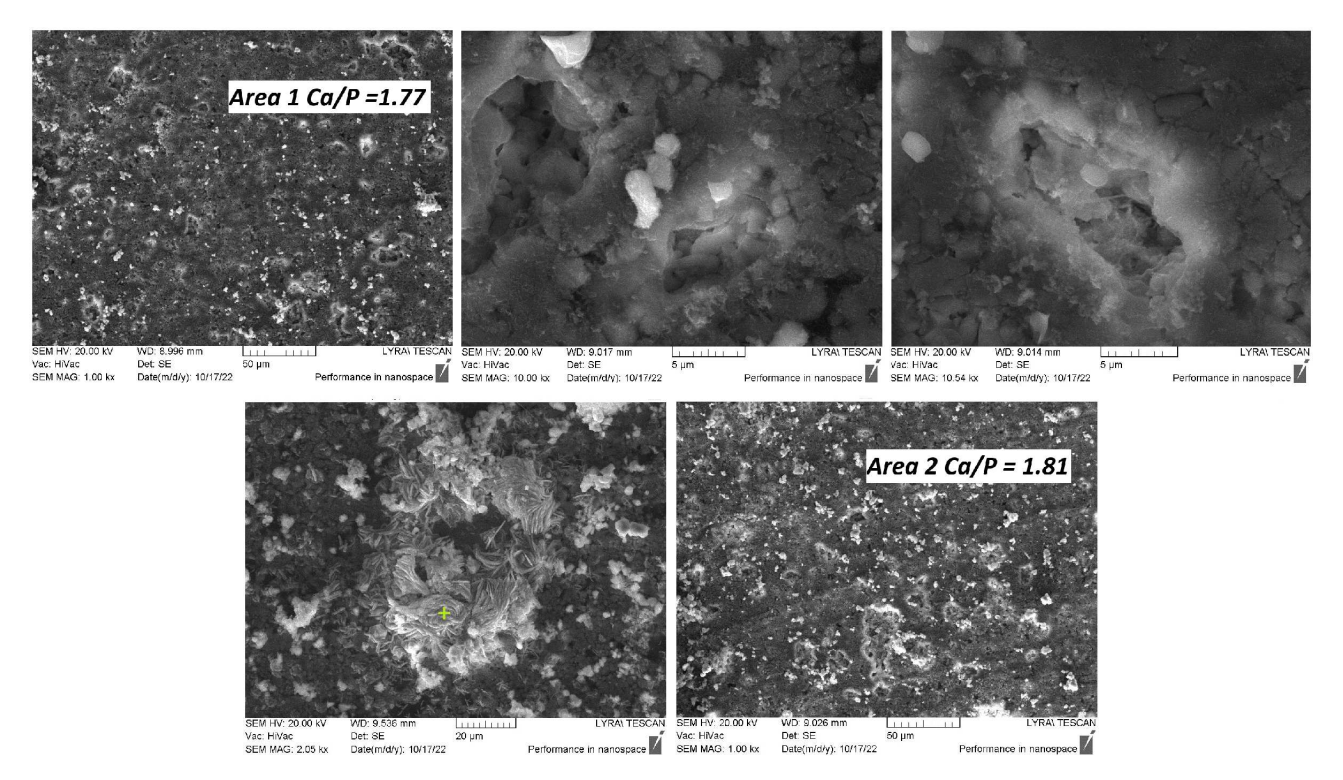


Figure 8. SEM images (different areas and magnifications) of the BHA after 21 days in SBF

stages, followed by the formation of Ca-rich deposits. The subsequent decrease to Ca/P = 1.75 at day 7 indicates dynamic ion exchange and structural reorganization. By day 21, the ratio changes only slightly ($\sim 1.77-1.81$), maintaining values slightly above the stoichiometric level (Ca/P = 1.67). Such behaviour is typical for bioactive BHA derived from natural materials [1–3].

IV. Conclusions

A comprehensive suite of analyses (FTIR, Raman, SEM-EDS and ICP-AES) has demonstrated the *in vitro* bioactivity of biogenic hydroxyapatite (BHA) derived from *Rapana venosa* shells in simulated body fluid (SBF).

Immersion in SBF induced progressive surface transformation of the synthesized BHA - from initially moderate activity, through active nucleation and deposition stages, to the formation of a stable, biologically relevant apatite layer. Although the BHA retained the ionic diversity of their raw material composition, the Ca/P ratio approached stoichiometric values characteristic of BHA, confirming their excellent bioactivity. The morphological changes observed via SEM underscore the material's ability to induce apatite mineralization *in vitro*, suggesting strong potential for osseointegration.

Acknowledgement: This study is funded by the European Union-Next Generation EU, through the National Recovery and Resilience Plan of the Republic of Bulgaria, project No. BG-RRP-2.004-0002, "BiOrgaMCT" (Bioactive Organic and Inorganic Advanced Materials and Clean Technologies).

References

- G.T. Tihan, V. Sereanu, A. Meghea, G. Voicu, M.G. Albu, V. Mitran, A. Cimpean, R.G. Zgârian, "Innovative methodology for developing a bone grafting composite biomaterial starting from the seashell of Rapana thomasiana", Comptes Randus Chimie, 20 (2017) 440–445.
- L.M. Cursaru, M. Iota, R.M. Piticescu, D. Tarnita, S.D. Savu, I.D. Savu, G. Dumitrescu, D. Popescu, R.-G. Hertzog, M. Calin, "Hydroxyapatite from natural sources for medical applications", *Materials*, 15 (2022) 5091.
- H.Y. Ahmed, N. Safwat, R. Shehata, E.H. Althubaiti, S. Kareem, A. Atef, S.H. Qari, A.H. Aljahani, A.S. Al-Meshal, M. Youssef, R. Sami, "Synthesis of natural nanohydroxyapatite from Snail shells and its biological activity: Antimicrobial, antibiofilm, and biocompatibility. *Membranes*, 12 (2022) 408.
- S. Kowalski, W. Gonciarz, R. Belka, A. Góral, M. Chmiela, Ł. Lechowicz, W. Kaca, W. Z' órawski, "Plasmasprayed hydroxyapatite coatings and their biological properties", *Coatings*, 12 (2022) 1317.
- B.R. Heimann, "Plasma-sprayed osseoconductive hydroxylapatite coatings for endoprosthetic hip implants: Phase composition, microstructure, properties, and biomedical functions", Coatings, 14 (2024) 787.
- C. Cimpeanu, D. Predoi, C.S. Ciobanu, S.L. Iconaru, K. Rokosz, M.V. Predoi, S. Raaen, M.L. Badea, "Development of novel biocomposites with antimicrobial-activitybased magnesium-doped hydroxyapatite with amoxicillin", *Antibiotics*, 13 (2024) 963.
- 7. U. Daood, A. Fawzy, "Development of a bioactive dentin adhesive resin modified with magnesium-doped synthetic hydroxyapatite crystals", *J. Mech. Behav. Biomed. Mater.*, **140** (2023) 105737.
- 8. R. Zhao, X. Meng, Z. Pan, Y. Li, H. Qian, X. Zhu, X. Yang, X. Zhang, "Advancements in nanohydroxyapatite:

- synthesis, biomedical applications and composite developments", *Regener. Biomater.*, **12** (2025) rbae129.
- C.S. Ciobanu, D. Predoi, S.L. Iconaru, K. Rokosz, S. Raaen, C.C. Negrila, L. Ghegoiu, C. Bleotu, M.V. Predoi, "Chrome doped hydroxyapatite enriched with Amoxicillin layers for biomedical applications", *Coatings*, 15 (2025) 233.
- D. Predoi, S.L. Iconaru, S.C. Ciobanu, S. Tălu, S.A. Predoi, N. Buton, G.Q. Ramos, H.D. da Fonseca Filho, R.S. Matos, "Synthesis, characterization, and antifungal properties of chrome-doped hydroxyapatite thin films", *Mater. Chem. Phys.*, 324 (2024) 129690.
- 11. Q.-X. Zhu, L. Liu, W.-T. Xu, Q.-Y. Nie, Y.-L. Xu, J.-X. Liu, "Fluorine substituted hydroxyapatite microspheres: Template-free hydrothermal synthesis and sustained fluoride-releasing properties", *Process. Appl. Ceram.*, 17 [3] (2023) 248–255.
- P.A. Forero-Sossa, I.U. Olvera-Alvarez, J.D. Salazar-Martinez, D.G. Espinosa-Arbelaez, B. Segura-Giraldo, A.L. Giraldo-Betancur, "Biogenic hydroxyapatite powders: Effects of source and processing methodologies on physicochemical properties and bioactive response", *Mater. Charact.*, 173 (2021) 110950–110964.
- E. Fiume, G. Magnaterra, A. Rahdar, E. Vernéand, F. Baino, "Hydroxyapatite for biomedical applications: A short overview, *Ceramics*, 4 (2021) 542–563.
- 14. I. Antoniac, A. Lesci, G. Blajan, A. Vitioanu, "Bioceramics and biocomposites from marine sources", *Key Eng. Mater.*, **672** (2015) 276–292.
- 15. M. Relva, Z. Benzarti, P. Faia, S. Carvalho, S. Devesa, "Biogenic synthesis of hydroxyapatite: A sustainable approach using Hylocereus undatus", *Ceram. Int.*, **51** [25] (2025) 44218–44230.
- 16. M. Akram, R. Ahmed, I. Shakir, W.A.W. Ibrahim, R. Hussain, "Extracting hydroxyapatite and its precursors from natural resources", *J. Mater. Sci.*, **49** (2014) 1461–1475.
- 17. D. Milovac, G. Gallego Ferrer, M. Ivankovic, H. Ivankovic, "PCL-coated hydroxyapatite scaffold derived from cuttlefish bone: Morphology, mechanical properties and bioactivity", *Mater. Sci. Eng. C*, **34** (2014) 437–445.
- 18. V.P. Sampath, V. Krishnasamy, "Synthesis and characterization of hydroxyapatite self-assembled nanocomposites on graphene oxide sheets from seashell waste: A green process for regenerative medicine". *J. Mechan. Behavior Biomed. Mater.*, **151** (2024) 106383.
- 19. T. Kokubo, H. Takadama, "How useful is SBF in predicting in vivo bone bioactivity?", *Biomaterials*, **27** (2006) 2907–2915.
- 20. A.A. Zadpoor, "Relationship between in vitro apatite-forming ability measured using simulated body fluid and in vivo bioactivity of biomaterials", *Mater. Sci. Eng. C*, **35** (2014) 134–143.
- D.J. Patty, A.D. Nugraheni, I.D. Ana, Y. Yusuf, "Mechanical characteristics and bioactivity of nanocomposite hydroxyapatite/collagen coated titanium for bone tissue engineering", *Bioengineering*, 9 (2022) 784.
- 22. M. Vallet-Regí, "Evolution of biomaterials", *Front. Mater.*, **9** (2022) 864016.
- M. Vallet-Regí, P. Esbrit, A.J. Salinas, "Degradative effects of the biological environment on ceramic biomaterials", *Biomater. Sci.*, 4 (2020) 955–971.
- 24. S. Hussain, Z.A. Shah, K. Sabiruddin, A.K. Keshri, "Characterization and tribological behaviour of Indian clam

- seashell-derived hydroxyapatite coating applied on titanium alloy by plasma spray technique", *J. Mech. Behavior Biomed. Mater.*, **137** (2023) 105550.
- S. Hussain, K. Sabiruddin, P. Patidar, K. Solanki, M.S. Baig, "In vitro bioactivity and biocompatibility behaviour of atmospheric plasma sprayed Indian clam *seashell* derived hydroxyapatite coating on Ti-alloy", *J. Alloys Compd.*, 976 (2024) 173132.
- 26. S.J. Jeyakumar, A. Sindhya, M. Jothibas, "A comparative study of surface modified nanohydroxyapatite using PVA polymer extracted from seashells, coral skeletons and eggshells for biomedical applications", *Surf. Interfaces*, **42** (2023) 103401.
- 27. J. Mateeva, A. Yoleva, S. Djambazov, "Phase study of Rapana Venosa shells from the Black Sea", *J. Chem. Technol. Metal.*, **58** [1] (2023) 38–43.
- 28. A. Yoleva, I. Mihailova, S. Djambazov, "Solid-state synthesis of hydroxyapatite from Black Sea Rapana Venosa shells", *J. Chem. Technol. Metal.*, **58** [2] (2023), 385–393.
- M. Ravi, B. Murugesan, A. Jeyakumar, K. Raparthi, "A review on utilizing the marine biorefinery waste in construction raw materials to reduce land pollution and enhance green environment", Adv. Mater. Sci., 21 (2021) 44–62.
- 30. A. Naqshbandi, A. Rahman, "Sodium doped hydroxyapatite: Synthesis, characterization and zeta potential studies", *Mater. Lett.*, **312** (2022) 131698.
- 31. O.A. Osuchukwu, A. Salihi, I. Abdullahi, D.O. Obada, "Synthesis and characterization of sol–gel derived hydroxyapatite from a novel mix of two natural biowastes and their potentials for biomedical applications", *Mater. Today Proc.*, **62** (2022) 4182–4187.
- E.S. Akpan, M. Dauda, L.S. Kuburi, D.O. Obada, N.D. Bansod, D. Dodoo-Arhin, "Hydroxyapatite ceramics prepared from two natural sources by direct thermal conversion: From material processing to mechanical measurements", *Mater. Today Proc.*, 38 (2021) 2291–2294.
- 33. V. Nosenko, N. Strutynska, I. Vorona, I. Zatovsky, V. Dzhagan, S. Lemishko, M. Epple, O. Prymak, N. Baran, S. Ishchenko, N. Slobodyanik, Y. Prylutskyy, N. Klyui, V. Temchenko, "Structure of biocompatible coatings produced from hydroxyapatite nanoparticles by detonation spraying", Nanoscale Res. Lett., 10 (2015) 464.
- 34. M. Arango-Ospina, A.R. Boccaccini, "Bioactive glasses and ceramics for tissue engineering", pp. 111–178 Ch. 4 in *Tissue Engineering Using Ceramics and Polymers (Third Edition)*. Eds. A.R. Boccaccini, P.X. Ma, L. Liverani. Woodhead Publishing, 2022.
- 35. S.G. Mtavangu, W. Mahene, R.L. Machunda, B. van der Bruggen, K.N. Njau, "Cockle (Anadara granosa) shells-based hydroxyapatite and its potential for defluoridation of drinking water", *Results Eng.*, **13** (2022) 100379.
- Y. Hou, A. Shavandi, A. Carne, "Marine shells: Potential opportunities for extraction of functional and health-promoting materials", *Critical Rev. Environm. Sci. Technol.*, 46 (2016) 1047–1116.
- 37. Z. Yao, M. Xia, H. Li, T. Chen, Y. Ye, H. Zheng, "Bivalve shell: not an abundant useless waste but a functional and versatile biomaterial", *Critical Rev. Environm. Sci. Technol*, **44** (2012) 2502–2530.
- 38. V. Lalzawmliana, A. Anand, P. Mukherjee, S. Chaudhuri, B. Kundu, S.K. Nandi, N.L. Thakur, "Marine organisms as a source of natural matrix for bone tissue engineering", *Ceram. Int.*, **45** [2] (2019) 1469–1481.

- 39. R. Rial, M. González-Durruthy, Z. Liu, J.M. Ruso, "Advanced materials based on nanosized hydroxyapatite", *Molecules*, **26** [11] (2021) 3190.
- 40. J. Morris, T. Backeljau, G. Chapelle, "Shells from aquaculture: a valuable biomaterial, not a nuisance waste product", *Rev. Aquacult.*, **11** (2019) 42–57.
- 41. Z. Zuliantoni, W. Suprapto, P. Setyarini, F. Gapsari, "Extraction and characterization of snail shell waste hydroxyapatite", *Results Eng.*, **14** (2022) 100390.
- 42. A. Dudek, L. Adamczyk, "Properties of hydroxyapatite layers used for implant coatings", *Optica Applicata.*, **43** (2013) 143–151.